AGU PUBLICATIONS

JGR

Journal of Geophysical Research: Solid Earth

RESEARCH ARTICLE
10.1002/2015JB012719

Key Points:
- Earthquake detection/relocation reveals pronounced migration in time, suggesting fluid trigger
- The *b* value evolution is connected to evolution of hypocentral structure
- Degree of fluid confinement within a fault zone may influence both hypocenters and *b* values

Supporting Information:
- Data Set S1
- Data Set S2
- Captions for Data Sets S1 and S2 and Captions for Movies S1–S3
- Movie S1
- Movie S2
- Movie S3

Correspondence to:
D. R. Shelly,
dshelly@usgs.gov

Citation:
Shelly, D. R., W. L. Ellsworth, and D. P. Hill (2016), Fluid-faulting evolution in high definition: Connecting fault structure and frequency-magnitude variations during the 2014 Long Valley Caldera, California, earthquake swarm, *J. Geophys. Res. Solid Earth*, *121*, doi:10.1002/2015JB012719.

Received 4 DEC 2015
Accepted 11 FEB 2016
Accepted article online 15 FEB 2016

Fluid-faulting evolution in high definition: Connecting fault structure and frequency-magnitude variations during the 2014 Long Valley Caldera, California, earthquake swarm

David R. Shelly[1], William L. Ellsworth[1,2], and David P. Hill[1]

[1]U.S. Geological Survey, Menlo Park, California, USA, [2]Department of Geophysics, Stanford University, Stanford, California, USA

Abstract An extended earthquake swarm occurred beneath southeastern Long Valley Caldera between May and November 2014, culminating in three magnitude 3.5 earthquakes and 1145 cataloged events on 26 September alone. The swarm produced the most prolific seismicity in the caldera since a major unrest episode in 1997–1998. To gain insight into the physics controlling swarm evolution, we used large-scale cross correlation between waveforms of cataloged earthquakes and continuous data, producing precise locations for 8494 events, more than 2.5 times the routine catalog. We also estimated magnitudes for 18,634 events (~5.5 times the routine catalog), using a principal component fit to measure waveform amplitudes relative to cataloged events. This expanded and relocated catalog reveals multiple episodes of pronounced hypocenter expansion and migration on a collection of neighboring faults. Given the rapid migration and alignment of hypocenters on narrow faults, we infer that activity was initiated and sustained by an evolving fluid pressure transient with a low-viscosity fluid, likely composed primarily of water and CO_2 exsolved from underlying magma. Although both updip and downdip migration were observed within the swarm, downdip activity ceased shortly after activation, while updip activity persisted for weeks at moderate levels. Strongly migrating, single-fault episodes within the larger swarm exhibited a higher proportion of larger earthquakes (lower Gutenberg-Richter *b* value), which may have been facilitated by fluid pressure confined in two dimensions within the fault zone. In contrast, the later swarm activity occurred on an increasingly diffuse collection of smaller faults, with a much higher *b* value.

1. Introduction

Earthquake swarms are sequences of sustained earthquake activity, not fitting a typical main shock-aftershock decay [*Mogi*, 1963]. Swarms are usually thought to be driven by external forcing that increases stress and/or reduces strength on seismogenic faults. Examples of such processes include aseismic slip, magmatic intrusion, and increases in pore fluid pressure. Elevated fluid pressure can trigger earthquakes on preexisting faults by decreasing the effective normal stress, thus reducing resistance to slip [*Hubbert and Rubey*, 1959]. Pore fluid pressure increases can be natural in origin [e.g., *Parotidis et al*., 2003; *Hill*, 2006], though, increasingly, examples are seen related to industrial fluid injection [e.g., *Healy et al*., 1968; *Horton*, 2012; *Frohlich*, 2012; *Ellsworth*, 2013; *Huang and Beroza*, 2015; *Benz et al*., 2015]. In most cases, fluids trigger the release of preexisting, dominantly tectonic stress (hydroshear); in extreme cases, where the fluid pressure exceeds the least compressive stress and differential stress is low, hydrofracturing (opening mode failure) becomes possible [*Sibson*, 1981; *Cox*, 2010]. Natural earthquake swarms are particularly common in volcanic and hydrothermal regions [*Hill*, 1977; *Sibson*, 1987; *Zaliapin and Ben-Zion*, 2013; *Fischer et al*., 2014], including Long Valley Caldera [*Hill*, 2006], where hydrous fluids may be supplied to the upper crust following exsolution from underlying magma [*Fournier*, 1999; *Martens and White*, 2013]. Similar conditions may generate swarms at other restless calderas, such as Yellowstone [*Waite and Smith*, 2002; *Shelly et al*., 2013b].

Long Valley Caldera was formed 760 ka with a cataclysmic eruption that ejected 600 km^3 of rhyolitic magma [*Hildreth*, 2004]. Subsequently, the caldera and associated volcanic field produced multiple smaller eruptions including the formation of Mammoth Mountain between 110 and 55 ka and a sequence of monogenic eruptions along Mono-Inyo volcanic chain, the most recent of which occurred ~200 years B.P. on Paoha Island in Mono Lake ~30 km north of the caldera [*Hildreth*, 2004]. In more recent years, since at least 1980 (when monitoring intensified), the caldera has been the locus of frequent unrest episodes, reflecting an

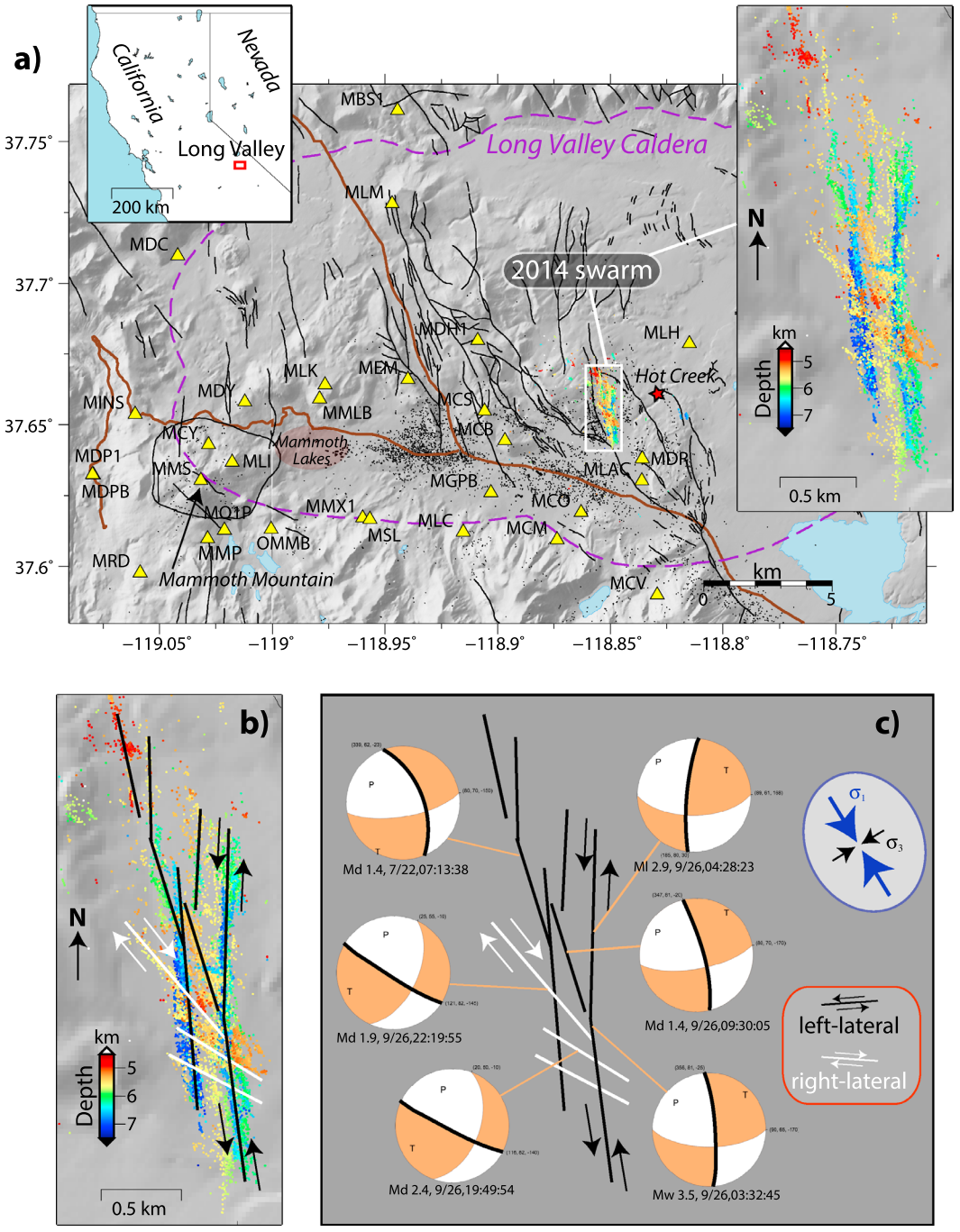

Figure 1. (a) Map of Long Valley Caldera and detected/relocated 2014 swarm activity (31 May to 1 November, dots colored by depth). All depths are referenced to mean station elevation, ~2.2 km above sea level. Black dots show relocated seismicity 1984–2011, *M* 2+ [*Waldhauser and Schaff*, 2008]. Yellow triangles are seismic stations used in this study—some are outside of mapped area. Thin black lines are mapped faults. Brown lines are roads. Purple dashed line shows caldera boundary. Left inset shows location of main map. Right inset shows zoomed view of the 2014 swarm events. (b) Map view of interpreted fault structure overlaid on earthquake locations. Black and white lines are interpreted left- and right-lateral structures, respectively. (c) Same interpreted structure with selected NCSN first-motion focal mechanisms to illustrate sense of slip. Interpreted fault plane is highlighted in bold. Faulting is dominantly left lateral strike slip, but later stage, relatively shallow activity included oblique right-lateral/normal faulting. Greatest (σ_1) and least (σ_3) principle stress orientations (inferred from this study and also consistent with *Prejean et al.* [2002]) are shown.

interaction of volcanic and tectonic processes [*Hill*, 2006]. Long Valley and the Sierra Nevada block immediately south were the sites of a series of four M ~6 earthquakes in late May 1980. Numerous earthquake swarms since that time include a major swarm in January 1983 (involving two M 5.3 events) and a large, extended-duration earthquake swarm in 1997–1998 [*Hill et al*., 2003; *Prejean et al*., 2002]. The 1980, 1983, and 1997–1998 episodes were all accompanied by rapid uplift of the central resurgent dome [*Hill*, 2006, and references therein]. More recently, slower uplift resumed at the resurgent dome during 2011–2014 [*Montgomery-Brown et al*., 2015]. At Mammoth Mountain, on the southwest rim of Long Valley Caldera, swarms are also common. Upper crustal swarms in 1989–1990 [*Hill and Prejean*, 2005; *Prejean et al*., 2003] and 2014 [*Shelly et al*., 2015], as well as deeper, lower crustal swarms [*Shelly and Hill*, 2011] have been interpreted as driven by CO_2-rich aqueous fluids, with fluctuations in surface CO_2 emissions showing correlation with deeper swarm activity [*Lewicki et al*., 2014].

The 2014 Long Valley earthquake swarm, which we examine here from 31 May through 1 November, was the most prolific swarm in the caldera since 1997–1998. The multistaged swarm occurred beneath the southeast margin of the caldera's resurgent dome, near the eastern edge of the most active seismic zone (Figure 1), with epicenters ~2 km west of the Hot Creek Geologic Site (Figure 1). The swarm included intense episodes on 7–8 July, and 25–27 September, peaking with three M 3.5 earthquakes on 26 September, with activity becoming shallower and more diffuse in space and time through October. In total, more than 3300 earthquakes from the sequence were included in the Northern California Seismic Network (NCSN) catalog, of which 1145 occurred on 26 September (UTC). Several of the larger swarm earthquakes were felt by residents of the nearby town of Mammoth Lakes (Figure 1). No long-period earthquakes were identified, and no change in surface deformation was detected during the swarm.

Here we seek to understand the physics and mechanics of rupture during this swarm. Toward this goal, we produce a high-resolution earthquake catalog by applying large-scale correlation-based earthquake detection and location techniques [*Shelly et al*., 2013a, 2013b]. This then allows us to constrain the relationships between the hypocentral structure, temporal evolution, and frequency-magnitude distribution evolution in ways not possible using a standard network catalog, or even a relocated catalog. In total, we leverage 3312 NCSN catalog earthquakes to create two new catalogs: a precisely located catalog containing 8494 earthquakes (~2.5 times the size of the NCSN catalog), and a larger superset catalog of 18,634 events (5.5 times the NCSN catalog) with magnitude estimates (but not necessarily with precise locations). Based on the observed spatial and temporal patterns of faulting, we infer that activity was related to fluid pressure perturbations in the seismogenic crust. As such, we also examine the interrelationship between faulting and fluid transport in the upper crust.

2. Methods

2.1. Event Detection and Relocation Procedure

We follow the event detection and location procedure described by *Shelly et al*. [2013a, 2013b], with minor modification as outlined below. The basic approach is to use routinely cataloged earthquakes to form waveform templates, which are then used to identify (and locate, if possible) uncataloged small earthquakes with similar waveforms via cross correlation with the multistation template. Since the newly identified earthquakes are similar to the template in waveform shape, differential times can be precisely measured using cross correlation. These differential times are input directly in a double-difference earthquake relocation algorithm (hypoDD) [*Waldhauser and Ellsworth*, 2000]. Thus, all earthquakes (catalog and newly detected) are relocated simultaneously, producing precise relative locations for both event types. The additionally detected earthquakes are important for illuminating details of swarm structures and activity patterns; their inclusion also potentially improves the relocation precision for the cataloged events, since the new events provide increased differential time linkage among swarm events.

Waveform templates were formed separately for P and S wave packets, beginning 0.25 s before the estimated phase arrival time, with durations of 2.5 s (P) or 4.0 s (S). If necessary (stations $<$ ~20 km distance), we truncated the P template to avoid overlapping with the S template. We formed templates using ground velocity time series, filtered 2–15 Hz, at stations with at least one (P or S) catalog phase pick, up to 50 km distance (Figure 1). If the second phase time was not picked, we predicted the arrival time using the catalog origin time and a P/S velocity ratio (v_p/v_s) of 1.65 (deliberately on the low side, to avoid missing the S wave onset

and thus potentially including the *S* arrival in the *P* template). We visually reviewed all templates and removed a small number (~6%, retaining 3105 template events out of 3312 total catalog events) due to multiple events within the template waveforms or obviously erroneous phase arrival times. Because of the long duration of this sequence (5 months), not all templates were scanned on all days. To balance computation and yield, we scanned each template on the day of its occurrence, as well as two days before and after. Additionally, each day was scanned by at least 60 template events (30 most recently prior to and following the day). Finally, all templates were scanned on four high seismicity days (7–8 July and 26–27 September), to ensure good connectivity among events in different stages of the swarm. If necessary, data were downsampled to 100 samples per second, and correlation values were calculated at increments of 1 sample (0.01 s).

In the process of scanning the template through continuous data using cross correlation, we also measured precise differential times for *P* and *S* templates across the network by interpolating the correlation function to subsample precision near its peak values using a simple three-point quadratic interpolation [*Shelly et al*., 2013a]. This achieves precision of ~1 ms (0.1 samples) for highly correlated waveforms, corresponding to ~3–7 m at typical seismic velocities. We set the maximum differential time as 0.5 s for *P* waves and 0.825 s for *S* waves—this is large enough to avoid "edge effects" (differential times commonly hitting up against the imposed limit), yet small enough to prevent template *P* waves from preferentially correlating with much higher amplitude *S* waves (i.e., erroneously giving differential *P* times of approximately the *S-P* time).

Here we adopt a couple of modifications to the previously employed technique [*Shelly et al*., 2013a, 2013b]. First, to accommodate events with different focal mechanisms (and thus different polarities at some stations), we measured differential times using the peak absolute value correlation (also done in *Shelly and Hill* [2011]). Second, we measured the height of the secondary peak absolute value correlation (at least 0.03 s away from the peak time) and used the difference between the peak and this secondary peak, cc_{diff}, as part of an empirical weighting function designed to capture confidence in the measurement. This weight, wt, was then used in the hypoDD relocation, calculated as follows:

$$wt = (0.1 + 3cc_{diff})cc_{max}^{2}, \quad (1)$$

where cc_{max} is the maximum (interpolated) correlation coefficient. Thus, measurements with both high correlation coefficient and a small secondary peak (large cc_{diff}) were weighted most strongly. Only measurements exceeding a threshold cc_{max} were saved; the threshold was set to 7 times the median absolute deviation for the particular waveform channel over a particular day, or 0.8, whichever was smaller. Typical thresholds were ~0.4–0.6. In rare cases when more than 10,000 correlation values in a day for a given data channel exceed this initial threshold, the threshold was raised as necessary to reduce this number to 10,000.

We input all data into hypoDD, including differential times derived from catalog phase pick times, with the same 1-D layered velocity model as used by *Prejean et al*. [2002]. Although we measured correlation values, times, and amplitudes on all six components (three components at two levels) of the ~2 km deep borehole [*Prejean and Ellsworth*, 2001] (station MDH1, Figure 1) and tested its inclusion in location estimates, this station was excluded from the final location inversion, due to large residuals. A 3-D velocity model that properly accounts for the instruments' positions at depth may be required; we also observed prominent late-arriving phases (presumed reflections) for some events on this station that may have interfered with accurate differential time measurements. To constrain the overall structure, in the first few iterations we weighted the catalog data strongly and the correlation data weakly. In later iterations, we reversed this weighting hierarchy and successively decreased the distance over which correlation measurements were included. In total, we used more than 41 million differential times in the relocation, of which ~39 million were correlation-derived times. Finally, we retained only those events that we considered to be well located; in this case, we required at least 20 *P*, 20 *S*, and 50 total correlation-derived differential times be retained throughout the inversion. Because the final locations were dictated by the cross-correlation data, these locations reflect centroid rather than hypocenter locations, though these terms are used interchangeably in this manuscript because the distinction is usually minor. Perhaps counterintuitively, the largest events of the sequence are among the most poorly located, due to relatively few events of similar magnitude with which to form optimal correlation pairs [*Schaff et al*., 2004], combined with waveform clipping at some stations. Note that all depths are reported relative to mean station elevation, ~2.2 km above sea level.

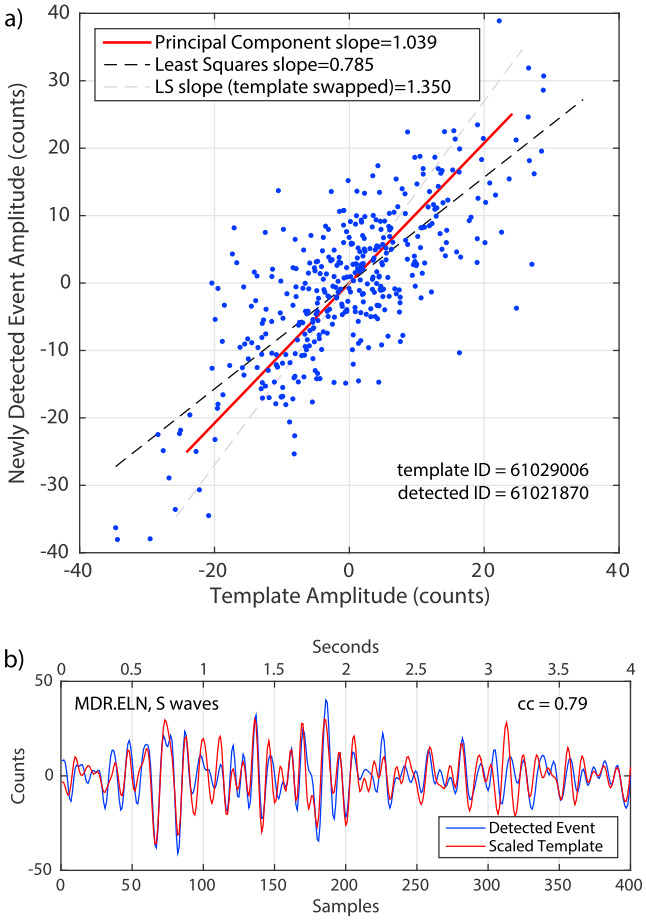

Figure 2. Example of relative amplitude estimation for detected and template waveforms (station MDR, ELN component). (a) Amplitudes of detected versus template waveforms for each sample (0.01 s). The principal component fit (red line) preserves the reciprocal relationship, but the least squares solution (black dashed line) is biased, showing lower apparent amplitude of the detected event, due to imperfect correlation [*Schaff and Richards*, 2014]. Gray dashed line shows the reciprocal relationship, where the least squares fit is repeated with the axes swapped (assuming the detected event was the template). (b) Plot of corresponding template and detected waveform time series. Template waveforms are scaled by 1.039, according to the relative amplitude estimated by the principal component fit. Correlation coefficient (cc) between the waveforms is 0.79.

2.2. Magnitude Estimation

The prospect of estimating magnitudes for newly detected events appears simple at first yet becomes nuanced in practice. Most recent studies that identify previously uncataloged events using a template-matching approach estimate the magnitude of the new event (M_{new}) based on the magnitude of the template event ($M_{template}$) using some variation of the following expression:

$$M_{new} = M_{template} + c\log_{10}(\alpha), \quad (2)$$

where α is the ratio of the newly detected and template event amplitudes [e.g., *Schaff and Richards*, 2014] and c is a constant that describes the amplitude-magnitude scaling. These parameters are explored in detail below.

2.2.1. Measuring Relative Event Amplitudes

Many strategies have been employed to measure relative amplitudes among events. A simple approach is to use peak amplitudes [e.g., *Huang and Beroza*, 2015], but peak values are inherently noisy. A much more robust technique is to use

$$\alpha = (x\,y)/(x\,x) \quad (3)$$

where $\boldsymbol{x}$ is the template waveform vector and $\boldsymbol{y}$ is the corresponding newly detected waveform [e.g., *Gibbons and Ringdal*, 2006; *Benz et al.*, 2015]. This is akin to a least squares fit to the relative amplitudes. While this approach works well when using a template with very high signal-to-noise and a detected event with identical waveform shape (excepting noise), it does not preserve the reciprocal relationship in that relative amplitudes are different if "template" and "new" events are swapped. In fact, as examined by *Schaff and Richards* [2014], any degradation in waveform similarity produces a biased (small) estimate for the magnitude of the newly detected event (Figure 2). A further option for dissimilar events is to estimate the relative amplitudes using the ratio of the L2 norms; however, this measure is not appropriate for very low signal-to-noise ratio (SNR) events [*Schaff and Richards*, 2014].

Considering these trade-offs, we adopt a modification to the above strategies. In order to reduce bias for somewhat dissimilar events yet maintain reasonable estimates for low SNR events, we estimate α using a principal component fit to the data vectors (Figure 2). Here

$$\alpha = v(2)/v(1), \quad (4)$$

where $v(1)$ and $v(2)$ are elements of the eigenvector $\boldsymbol{v}$ corresponding to the largest eigenvalue of the covariance matrix of $\boldsymbol{x}$ and $\boldsymbol{y}$, Cov($\boldsymbol{x}$,$\boldsymbol{y}$). We note that this is computationally similar to the method of *Rubinstein and*

Ellsworth [2010] for calculating relative amplitudes within repeating earthquake families via singular value decomposition; however, it differs in application because that technique required groups of nearly identical earthquakes, while here the advantage is instead for pairs of somewhat dissimilar earthquakes.

Rather than minimizing misfit in the *y* axis direction only (as with a least squares fit), a principal component fit (sometimes referred to as total least squares) minimizes misfit perpendicular to the best fitting line, without assigning dependent and independent variables. Thus, unlike a least squares fit, the principal component fit preserves the logical relationship whereby the estimated slope for event *y* versus event *x* is the reciprocal of event *x* versus event *y*. Figure 2 compares relative amplitudes estimated by principal component analysis with those from least squares. For this example with two similarly sized but imperfectly correlated (correlation coefficient of 0.79) events, the least squares fit suggests that whichever is the nontemplate is ~25% lower in amplitude, while the principal component correctly shows the events to be very similar in amplitude, independent of which is considered the template.

We make these relative amplitude measurements on the template and corresponding detected waveforms each station, component, and phase for which the correlation coefficient exceeds threshold (see details above), using the seismic velocity time series filtered 2–15 Hz. We then combine these measurements into a single estimate of α by taking the median of all values for the event pair. After converting this α to a magnitude estimate for the newly detected event (see below), we finally assign the event magnitude as the median of the magnitudes estimated individually from all template events detecting the given event. Direct comparison to many events at many stations, combined with median averaging, provides more redundancy for these magnitude estimates compared to catalog magnitudes.

2.2.2. Amplitude-Magnitude Scaling

Before we complete this process and estimate a magnitude, we need to determine a value for *c*. The choice of *c* is more complex than it initially appears. Many studies, by analogy with the procedure for local magnitude (M_L, which is defined as being proportional the logarithm of the amplitude on a Wood-Anderson seismograph), simply take $c = 1$ [e.g., *Schaff and Richards*, 2014; *Huang and Beroza*, 2015; *Benz et al*., 2015]. However, given that we are working with relatively small events, whose corner frequencies dominantly lie above our band-pass range of 2–15 Hz, the measured amplitude ratio for this band-passed data should, in fact, faithfully reflect the ratio of seismic moments [e.g., *Hanks and Boore*, 1984; *Bakun*, 1984]. Therefore, we could alternately use the scaling defined for moment magnitude (M_w), in which case $c = 2/3$ [*Hanks and Kanamori*, 1979].

This discrepancy in the appropriate value of *c* for M_L ($c \approx 1$) or M_w ($c \approx 2/3$) highlights the deviation between these magnitude scales at small magnitudes [*Hanks and Boore*, 1984]. Although moment magnitude (M_w) has been calibrated to approximate M_L for moderate magnitude earthquakes (M ~3–6), at small magnitudes ($<$~M 3) the relationship between log moment and M_L is found to change in slope, approaching a slope of 1.0 for very small earthquakes as the amplitudes begin to be measured below the corner frequencies [*Hanks and Boore*, 1984] or perhaps related to scale-dependent stress heterogeneity [*Ben-Zion and Zhu*, 2002]. This leads to a large discrepancy between M_L and M_w at very small magnitudes. Studies that have looked at the relationship between M_L and seismic moment in detail have supported this, for example, finding equivalent *c* values for M_L of 5/6 (for M_L 1.5–3.5 events in California [*Bakun*, 1984]) or 0.95 (M_L 0.3–3.0 events in Western Bohemia [*Hainzl and Fischer*, 2002]), both significantly greater than the 2/3 slope defined for M_w. Further complicating the issue is that the vast majority of events from the 2014 Long Valley swarm have only duration magnitude (M_d) estimates designed to approximate local magnitude [*Eaton*, 1992] with local magnitudes [*Uhrhammer et al*., 2011] or moment magnitudes only calculated for a few of the largest ($M_w > 3$) events in this sequence.

Although future work could reestimate all event magnitudes as M_w [e.g., *Cleveland and Ammon*, 2015], at this stage we elect to extend, rather than replace, the network magnitudes. Thus, cognizant of the trade-offs, we adopt the pragmatic approach of empirically matching catalog magnitude scaling and extending this scaling to newly detected events. To do this, we examine each pair of template (catalog) events for which we have made relative amplitude measurements. We plot the differential catalog (duration) magnitude versus the logarithm of our median amplitude ratio, α (Figure 3). The relationship is remarkably linear overall. Two minor deviations from the overall trend can be seen. The first is a slightly increased slope at large magnitude differences, which are the rare measurements pairing the very largest and smallest catalog events. This could

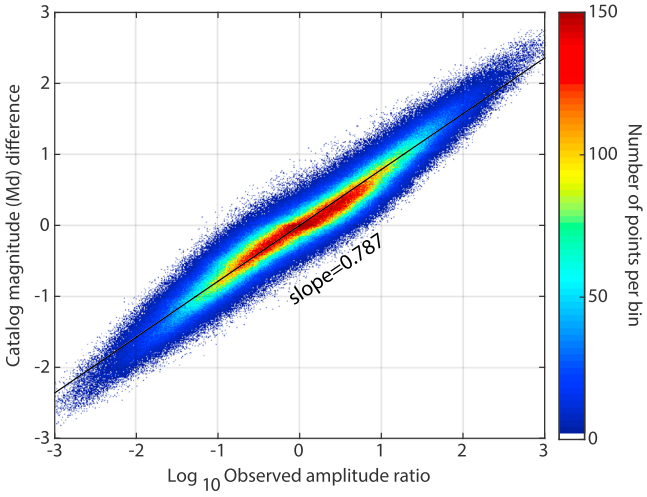

Figure 3. Magnitude calibration showing the relationship between observed amplitude ratios and differential NCSN (duration) magnitudes for pairs of catalog earthquakes. The best fitting slope is 0.787 (determined by a robust linear fit using a bisquare weighting function). This value is intermediate between the scaling expected for moment magnitude, M_w, (slope of 2/3) and local magnitude, M_L, (slope of 1) in this magnitude range (see text). Color shows density of observations at a given point. Inflection at zero magnitude difference suggests the existence of "preferred" catalog magnitudes (see Figure 7).

reflect bias from occasional clipping or lower corner frequencies for large (i.e., $M > 3$) events (see above), or alternatively could derive from a bias in catalog magnitude for the smallest events, beyond the range where duration magnitudes have been calibrated [*Eaton*, 1992]. The second deviation is a decreased slope near zero magnitude difference. This suggests a possible catalog magnitude artifact whereby certain magnitudes may be preferentially assigned, resulting in a smaller apparent difference in magnitude for events of different size. Given the inherent uncertainties, a simple linear relationship remains most appropriate. Using a robust linear fit to minimize the influence of outliers, we determine a best fitting slope of 0.79 (intermediate between the expectations for M_L and M_w at small magnitudes), which we assign to c (equation (2)). We term these magnitudes "extended duration magnitudes" (M_{dext}). We note that in addition to altering the magnitudes themselves, the choice of c has significant implications for the estimated Gutenberg-Richter b value, which scales inversely with c.

We produce a larger event magnitude catalog than the catalog with precise locations. This is possible because the magnitude can be reliably measured using the typically larger amplitude S phase alone, but we mandate both P and S differential time measurements for inclusion in the precisely located catalog. We require at least 15 S phase and 30 total correlation-derived differential times for inclusion in the magnitude catalog. These criteria weed out most artifacts (such as occasional spurious events resulting from template P waves weakly correlating with continuous S waves), producing a magnitude data set of 18,634 events.

2.3. Gutenberg-Richter *b* Value Estimation

One of the best known descriptions of earthquake statistics is the Gutenberg-Richter distribution, which describes the relative numbers of small and large earthquakes as $\log(N) = a - bM$ [*Ishimoto and Iida*, 1939; *Gutenberg and Richter*, 1942]. Here N is the cumulative number of earthquakes larger than a given magnitude (or alternatively, the number of earthquakes in a given magnitude bin), a describes the rate of earthquakes at or above $M = 0$, and b is a constant that describes the relative proportions of small and large earthquakes.

Throughout the manuscript, we use the maximum-likelihood method of *Tinti and Mulargia* [1987] to estimate b values and corresponding uncertainties. We also tested similar methods for b value estimation [*Utsu*, 1966; *Bender*, 1983] and uncertainty [*Shi and Bolt*, 1982] and found very similar results. All of these methods account for magnitude binning (the rounding of magnitude values), although this effect is relatively minor with the binning increment of 0.01 used in this manuscript. An instructive summary of these methods is provided by *Marzocchi and Sandri* [2003]. We use a cutoff magnitude $M_c = -0.4$, derived using a widely applied maximum curvature method [*Wiemer and Wyss*, 2000] with an upward adjustment of 0.2 magnitude units suggested by *Woessner and Wiemer* [2005]. M_c is sometimes called the completeness magnitude, but we deliberately avoid that description here because, as we see later, we do not actually expect full completeness at this magnitude, at least not without applying a correction (see section below for details). To avoid spurious fluctuations in the estimated b value, we use a conservative minimum of 1000 events above M_c for each b value estimate presented in this study, corresponding to uncertainty of ~0.02–0.03 for the range of b values (~0.6–1.0) found here.

As mentioned above, the choice of magnitude type has significant implications for the estimated b value from populations of small events. For very small events, the estimated b value may be up to 50% higher when using M_w compared to M_L. In fact, given that M_L is expected to scale directly with the logarithm of the seismic moment, a b value derived from M_L is perhaps more akin to the β parameter relating frequency and moment (M_0), $\log(N) = a - \beta\log(M_0)$, where $b = 1.5\beta$ [*Wyss*, 1973; *Kagan*, 1991; *Utsu*, 1999]. In this study, we extend the magnitude scale in a manner consistent with catalog M_d, producing a scaling that appears to be intermediate between these extremes. Nevertheless, for comparison with studies using M_w, b values from this study should probably be multiplied by $0.79/(2/3) \approx 1.2$. As with many studies we emphasize relative b values, rather than the absolute values.

2.3.1. Incompleteness Correction

During times of high seismicity rate, the detected events begin to consume a significant portion of the total time, resulting in incomplete detection. Because we enforce a minimum 4 s separation at the initial detection stage, for each detection up to 8 s (4 before the event and 4 after) are then unavailable to detect additional events. To account for this effect, we find the fraction of detector time available for detecting events at a given magnitude within ±1 h of each event, simply assuming that the event rate at a given magnitude remains the same during the time when such events are undetectable. Assuming that the largest of simultaneous events will preferentially be detected (or at least that the estimated magnitude will reflect that of the largest event), the completeness as a function of magnitude M can be estimated as the total time minus the time consumed by events of greater magnitude. Thus,

$$\text{completeness}(M) = 7200 - 8n_M, \tag{5}$$

where n_M is the number of events above the magnitude of interest within a 2 h (7200 s) window centered on the event time. In one sense, this is an upper bound because events can be separated by as little as 4 s, thus excluding less time for remaining events, but this effect is balanced against coda durations that exceed 4 s for some events. The choice of ±1 h is somewhat arbitrary but reasonable—longer time windows would reduce the correction but would also fail to capture short-term event rate variability.

2.3.2. The *b* Value Correction

We correct b values using the expected completeness measure described above, by weighting each observed event in the maximum-likelihood estimate by the inverse completeness at the observed magnitude at the observed time. For example, if we observe an M −0.2 event at a time where the completeness at this magnitude is estimated at 50%, we calculate the corrected b value assuming that two M −0.2 events actually occurred. Thus, we do not create event magnitudes that are not actually observed—we simply adjust their rate to account for the fraction of time when such events are undetectable. Similarly, in frequency-magnitude plots, we multiply the number of observed events in each magnitude bin by the reciprocal event-averaged completeness at that magnitude. Although this correction is important to apply and has a significant effect on b values during the very high activity rate times periods, the results are not terribly sensitive to the details of the correction, since b value variations only depend on the differential completeness on a logarithmic scale. We use M_c estimated from the original distribution and do not adjust the value here—however, we note that had we not corrected the distribution for the expected completeness, we would be missing a significant percentage of events above our determined M_c—this is the reason for referring to M_c as the "cutoff" rather than "completeness" magnitude.

3. Results and Discussion

As discussed above, we produce two catalogs: a precisely located catalog of 8494 events and a superset catalog with magnitudes only, which contains 18,634 events. Both catalogs are included in the supporting information.

3.1. Earthquake Locations

Precise locations reveal a mix of simplicity and complexity in faulting structure. On a short timescale, individual episodes often form nearly planar structures with north striking, left-lateral slip on near-vertical (or very steeply east dipping) faults (Figure 1). Two main subparallel fault zones, separated by ~300 m, were activated in this orientation, the westward strand on 7–8 July and the eastern strand on 25–26 September (Figure 4 and supporting information Movies S1 and S2).

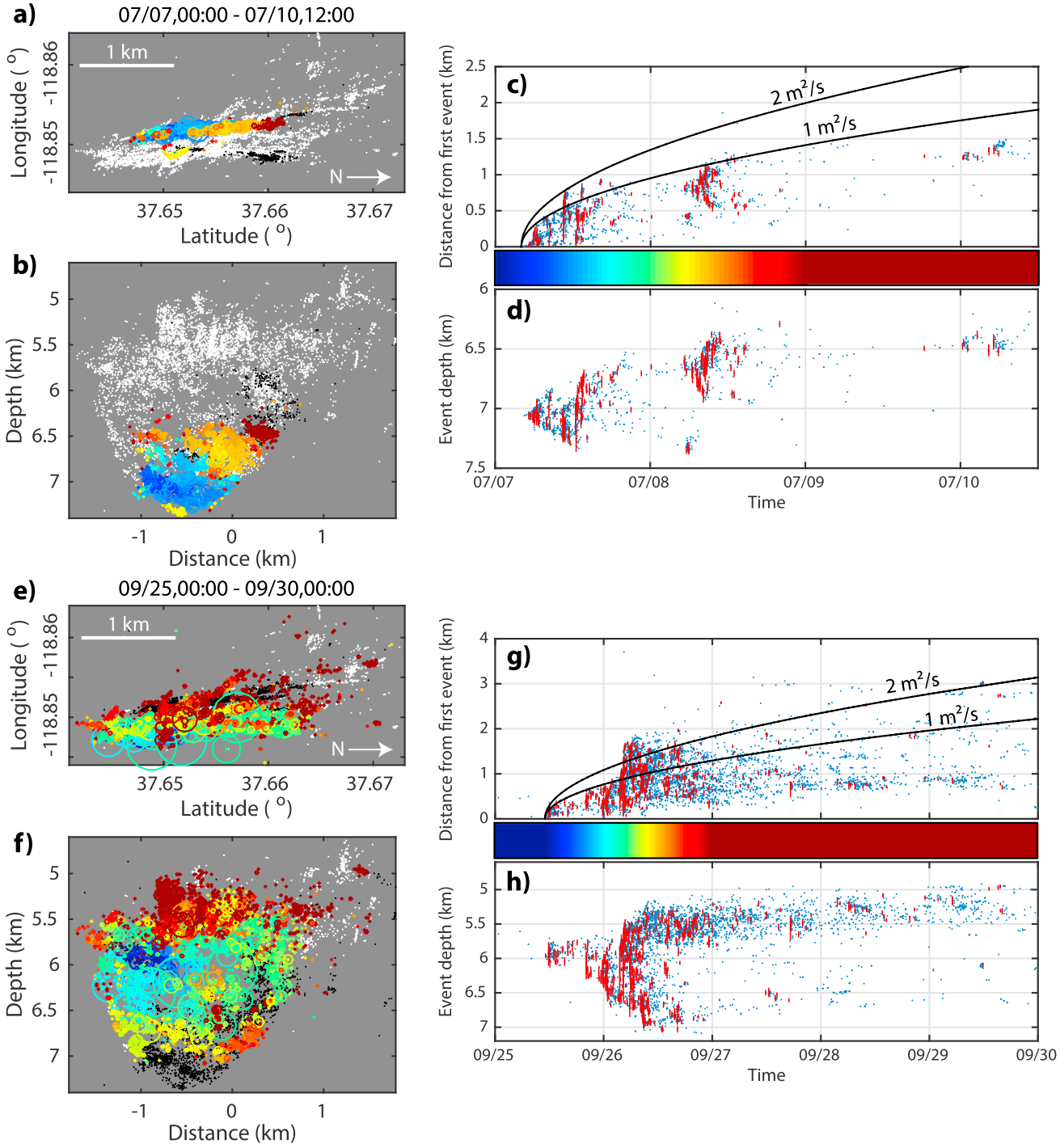

Figure 4. Swarm migration. Upper group shows example from 7 to 10 July. (a) Rotated map view. Color scale is at right. Events during the remaining (31 May to 1 November 2014) swarm outside the specified time range are plotted in black (events before window) or white (events after window). Circles show estimated rupture dimensions for $M \geq 1$ earthquakes, assuming 3 MPa stress drop. (b) Corresponding (south to north) cross section. Depths referenced to mean station elevation, ~2.2 km above sea level. (c) Distance (in three dimensions) from the first event with time. Diffusivity values of 1 and 2 m^2/s (according to the *Shapiro et al.* [1997] definition) are plotted for reference. Red bars show estimated finite rupture dimension as in Figures 4a and 4b. (d) Depth versus time. (e–h) Same as Figures 4a–4d, but for the 25–29 September sequence. See also supporting information Movies S1–3.

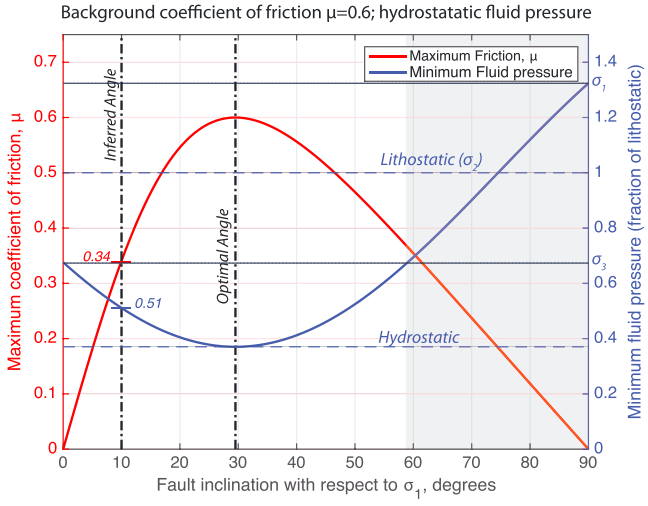

Figure 5. Upper bound effective friction (red) and corresponding lower bound fluid pressure (blue, fraction of lithostatic pressure), for slip to occur as a function of the fault angle with the direction of greatest principal stress, σ_1 [see *Hill*, 1993]. Plot assumes a "strong crust" model with cohensionless faults, where, in general, $\mu = 0.6$, fluid pressure is hydrostatic. Failure on faults deviating from the optimal orientation (~30° from σ_1) then requires either unusually low friction or high fluid pressure on these suboptimally oriented faults. This example is for a pure strike-slip regime, where σ_2 is the vertical (lithostatic) stress. Blue dotted lines show other principal stress levels. Shaded area at right is domain for which fluid pressure above σ_3 (or very low intrinsic friction) would be required for failure. For the 2014 Long Valley swarm, we infer some faults are activated within 10° of σ_1 (see Figure 1). Assuming intrinsic friction is unchanged, this suggests that fluid pressure may be elevated to at least 51% of lithostatic pressure, 38% above the assumed background hydrostatic pressure.

Activation of two parallel strands may seem surprising from a stress standpoint, where slip on one fault would reduce stress on the parallel structure. However, upon inspection, the slip on these strands was complementary in cross section, with only minor overlap. The July sequence occurred mostly below 6.5 km depth, with some shallower activity on the northern edge (Figures 4a and 4b and supporting information Movies S1 and S3). The sequence in late September (including the three *M* 3.5 events) then filled in above this depth (Figures 4e and 4f and supporting information Movies S2 and S3). Subsequent deeper propagation of the September activity was probably driven by stress (and perhaps fluid) transfer from the adjacent shallower activity (supporting information Movie 2).

Later in the swarm, the structures activated became increasingly complex (Figures 4e and 4f and supporting information Movies S2 and S3). In addition to the dominant left-lateral, north striking faults, other structures of varying orientations are also revealed in the locations and focal mechanisms, including southeast striking, steeply southwest dipping faults on the updip edge (5–6 km depth—all depths referenced to mean station elevation of ~2.2 km above sea level), which apparently activated in an oblique normal/right-lateral sense (Figure 1). These left- and right-lateral fault systems are separated by as much as 60° and as little as 20° in strike. At 60° separation, both sets may be optimally oriented for failure at ±30° with respect to the maximum compressive stress (σ_1), if we adopt the simplifying assumption under Andersonian faulting theory that in a strike-slip regime, σ_1 is approximately horizontal [*Sibson*, 1985]. At 20° separation, however, one or both faults may be poorly oriented. Assuming these faults are operating under similar stress conditions, this implies that at least one fault strikes within 10° of the maximum compressive stress (σ_1) direction (Figure 1) and thus operates under low resolved shear stress. Under simplified Andersonian conditions where one principal stress is vertical, such faults would be poorly oriented for slip [*Sibson*, 1985], and failure would require low effective friction, likely related to high fluid pressure [*Terakawa et al.*, 2013]. Figure 5 explores the conditions that may be required for slip in a strike-slip regime (intermediate stress, σ_2, vertical) as function of fault angle with σ_1. Assuming hydrostatic fluid pressure and a friction coefficient (μ) of 0.6, the optimal angle for slip is ~30°. At 10° from σ_1, an effective coefficient of friction of 0.34 or lower would be required for slip on this structure (as opposed to an optimally oriented fault with $\mu = 0.6$). Assuming intrinsic friction is unchanged, fluid pressure of at least 51% of lithostatic (~38% above hydrostatic) would be required. At ~5 km depth, this would equate to a pressure increase of ~19 MPa above hydrostatic. Given other evidence for high fluid pressure, this condition seems reasonable, and the pressure remains well below the minimum compressive stress (σ_3) estimated in this analysis. In fact, this faulting structure is similar to that identified for the 2008 West Bohemia (Czech Republic) earthquake swarm, a sequence also interpreted to be fluid driven [*Vavryčuk et al.*, 2013, Figure 8]. An apparent normal-faulting component and steep SW dip of the oblique right-lateral events may partially compensate for a suboptimal orientation for the strike-slip component. Misoriented faults may also

be more likely to host mixed shear and tensile, non-double-couple earthquakes [*Vavryčuk*, 2002; *Fischer and Guest*, 2011].

In aggregate, with multiple faults at various orientations, the swarm begins to bear some resemblance to a fault mesh structure (Figure 1) [*Hill*, 1977; *Sibson*, 1996], yet the crossing faults are mostly separated in depth and therefore do not form a fully interconnected network. Despite likely fluid involvement, we do not see clear evidence for non-double-couple faulting, and *P* wave first motions are usually well fit by an assumed double-couple mechanism. Thus, mechanisms reflect dominant shear faulting; however, it is possible that at least some events contain non-double-couple components, given the limited resolution and the fact that such events have been reported in this area in the past [*Dreger et al*., 2000; *Foulger et al*., 2004]. Clear observation of non-double-couple mechanisms is challenged in part by the asymmetric network distribution (Figure 1). Although potential exists for a more detailed examination of focal mechanisms in the swarm, in this manuscript we focus primarily on event location and magnitude distributions.

3.2. Fluids and Migration

The 2014 Long Valley swarm sequence exhibited repeated episodes of migration, which were especially pronounced during the July and September subswarms (Figure 4). The migration sequences in July and September were qualitatively similar, beginning with small events in a small source zone and expanding dramatically outward with time (Figure 4 and supporting information Movies S1–S3).

The dramatic expansion of seismicity with time is probably a consequence of triggering by fluid pressure diffusion [e.g., *Hainzl*, 2004; *Shelly et al*., 2013b]. Indeed, we infer that the swarm as a whole was driven by a fluid pressure transient, with a low-viscosity fluid capable of traversing preexisting faults and fractures in the subsurface, taking advantage of large increases in permeability within the ruptured area of the fault [e.g., *Sibson*, 1981; *Barton et al*., 2009]. Most likely, these fluids are composed dominantly of water and CO_2, exsolved from underlying magma [e.g., *Seccia et al*., 2011]. Water and CO_2 eventually migrate toward the surface, following the hydraulic gradient. In the ductile regime, likely a short distance beneath the deepest swarm activity, aqueous fluids would be subjected to approximately lithostatic pressure. As these high-pressure fluids cross into the sublithostatic pressure brittle region, they raise the fluid pressure on preexisting faults, triggering earthquakes on those faults already near failure by reducing the effective normal (clamping) stress on these faults [*Fournier*, 1999; *Cox*, 2005].

Although magmatic injection is sometimes inferred to trigger earthquake swarms [e.g., *Hill*, 1977; *Ukawa and Tsukahara*, 1996; *White et al*., 2011; *Gudmundsson et al*., 2014], direct involvement of magma is unlikely in this case given the rapid migration exhibited in the swarm, suggesting equally rapid fluid pressure diffusion. This requires either a low-viscosity fluid or a wide-aperture conduit—the lack of either significant surface deformation or large-magnitude earthquakes argue that the latter is unlikely. A significant aperture would also be required for a magmatic dike to avoid freezing over the multimonth swarm duration.

Aseismic slip is similarly unlikely as the primary driver of this swarm. Swarms driven by aseismic slip usually trigger earthquakes by loading seismic asperities either within or at the edge of a creeping zone [e.g., *Linde et al*., 1996*; Ozawa et al*., 2003; *Segall et al*., 2006]. However, neither case explains the observed patterns in the 2014 Long Valley swarm. Earthquakes migrate outward along a fault in all directions from small initiation zones, so they do not seem to be on the edge of a creeping zone. Additionally, seismic slip during the swarm appears to cover the entire fault plane (Figure 4 and supporting information Movies S1–S3), so the earthquakes are not occurring on small asperities embedded within a mostly creeping fault. Thus, although aseismic slip could play a minor role in swarm evolution, there is no obvious location to host such slip as a larger-scale swarm driver.

Triggering by elevated fluid pressure, however, can explain the outward propagation of earthquakes from a small initial source zone. If we adopt the model of *Shapiro et al*. [1997], $r \leq \sqrt{(4\pi Dt)}$, where r is the distance of an earthquake from a point of fluid injection, t is time, and D is the diffusivity, $D \approx 1$–$2\ m^2/s$ fits both the July and September sequences relatively well (Figures 4c and 4g). These diffusivity values are similar to the 2009 Mount Rainier swarm (~$1\ m^2/s$) [*Shelly et al*., 2013a], the 2010 Yellowstone earthquake swarm (~$1.5\ m^2/s$) [*Shelly et al*., 2013b], and shorter bursts of the 2000 Vogtland/NW Bohemia swarm (0.3–$10\ m^2/s$) [*Parotidis et al*., 2003]. Somewhat lower diffusivity values have been reported for the 2000 and 2008 Vogtland swarms overall (~$0.3\ m^2/s$) [*Hainzl et al*., 2012], the 1989 Mammoth Mountain swarm (0.2–$0.8\ m^2/s$) [*Hill and Prejean*,

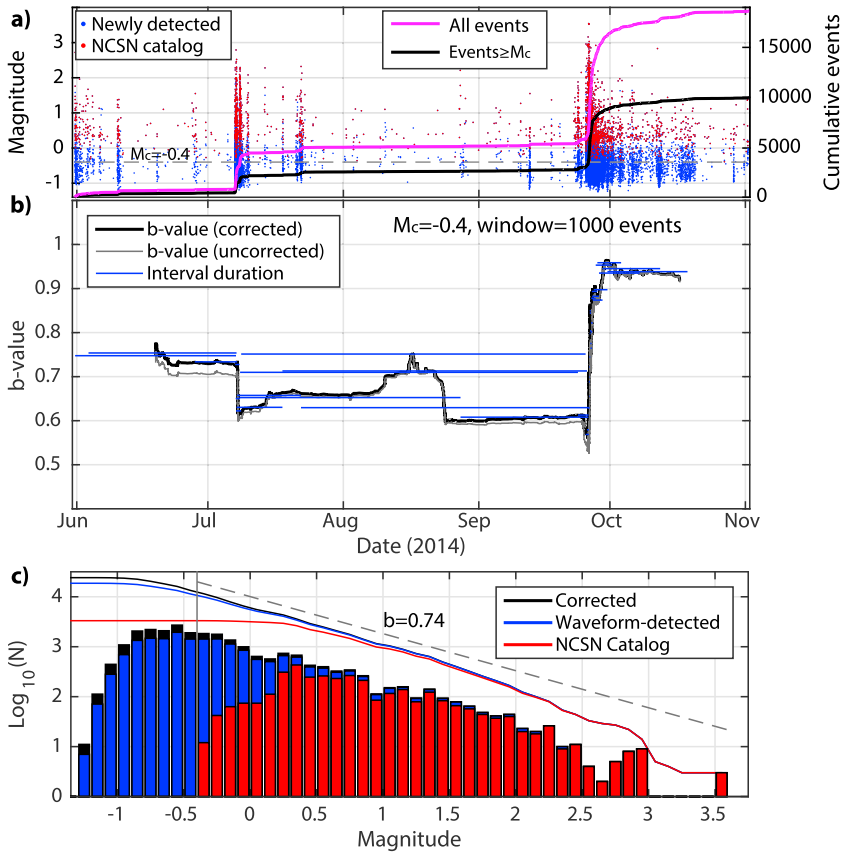

Figure 6. Frequency-magnitude distribution and associated variations in *b* value versus time. (a) Event magnitude versus time for NCSN catalog events (red dots) and newly detected events (blue dots). Lines show cumulative events with time for all events (magenta) and those larger than the cutoff magnitude of $M_c = -0.4$ (black), the latter of which are used in the *b* value estimation. (b) The *b* values versus time, calculated using a moving 1000 event window. Black line is corrected for times when the detector is blind due to other detections (see text). Gray line shows uncorrected value (see Figure 7). Blue horizontal bars show the time period encompassed by the windows at particular times. (c) Frequency-magnitude distribution for the entire sequence, showing NCSN catalog events (red), newly detected events (blue), and a correction for times when the detector is blind (black). Lines show corresponding cumulative distributions (all earthquakes greater than or equal to a given magnitude). The *b* value (dashed line) is estimated using the corrected distribution.

2005], and for a collection of earthquake swarms in Southern California (0.01–0.8 m^2/s) [*Chen et al.*, 2012]. However, while perhaps useful for comparison, the significance of such values is unclear, given that we expect the underlying assumption of homogeneous isotropic diffusion to be grossly violated, with permeability instead dominated by fractures and strongly affected by rupture [*Sibson*, 1981; *Barton et al.*, 2009; *McClure and Horne*, 2011]. Additionally, these comparisons assume that earthquakes in these disparate settings are triggered at similar fluid pressure perturbations, which need not be the case.

Rather than the earthquakes being a simple consequence of fluid diffusion, we expect the faulting and fluid pressure diffusion processes to be intimately and inextricably coupled [e.g., *Sibson*, 1981, 2001; *Cox*, 2005; *Ingebritsen and Manning*, 2010; *Shelly et al.*, 2015]. Even prior to faulting, preexisting fractures and fault zones likely serve as the primary fluid conduits in the subsurface. As fluid pressure rises, the first earthquakes will occur on faults already stressed near failure. With faulting, permeability is expected to increase dramatically, so that faulting may act as a "valve" whereby differing fluid pressure regimes on either end of the rupture would then equilibrate rapidly [*Sibson*, 1981]. When combined with stress transfer, this process likely drives the observed rapid expansion of activity [e.g., *Hainzl*, 2004], where earthquakes focus around the fringes of previous ruptures, as fluid pressure rises in this zone of stress concentration after the rupture (supporting information Movies S1 and S2). Larger events, such as the *M* 3.5 earthquakes that occurred as part of the 26 September sequence, likely facilitate especially rapid fluid diffusion, given their relatively large rupture areas and slip distances (Figure 4g) [*McClure and Horne*, 2011].

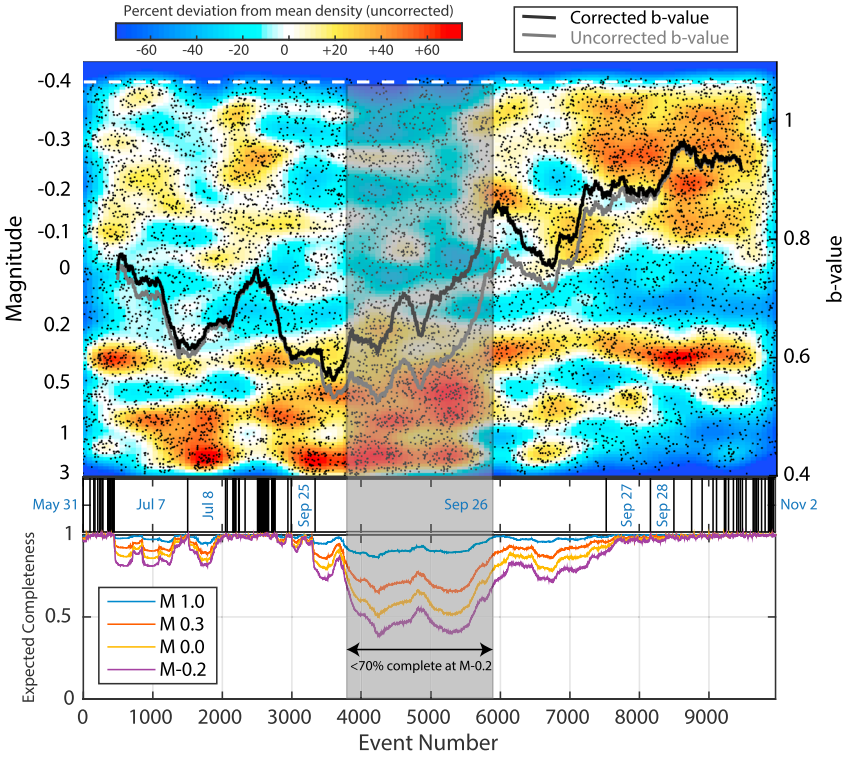

Figure 7. (top) Earthquakes above the cutoff magnitude $M_c = -0.4$ (black dots), sequentially with time (slight dithering is applied for plotting purposes [*Agnew*, 2015]). Magnitude axis is transformed for equal density with a *b* value of 0.7. Color shows corresponding deviation in event density, smoothed using a Gaussian kernel. Lines show *b* values using a 1000 event moving window (same as Figure 6b), using the raw enhanced catalog (gray) and correcting detector saturation time (see text and Figure 7 (bottom)) during high seismicity rates (black). (middle) Corresponding time, with a vertical black line separating each day. (bottom) Estimated completeness fraction at selected magnitudes, based on detector saturation time. Completeness is expected to be relatively poor during extremely high seismicity rates during part of September 26. Shaded area denotes time period when completeness is expected to be below 70% at M −0.2.

Another likely consequence of fluid-faulting interactions is displayed by the pattern of faulting depth versus time (Figures 4d and 4h). Although we observe a preference for upward migration overall, downward migration is also observed. This probably reflects local complexity in the hydraulic gradient, combined with preexisting stress on faults. Assuming that background fluid pressure is near hydrostatic in the shallower brittle regime, this leaves ample potential for downward fluid pressure diffusion, because a suprahydrostatic (e.g., 50% of lithostatic) fluid source at these depths could easily overcome the hydrostatic gradient over a small depth range. Similar downdip migration was seen in the 2010 Yellowstone swarm [*Shelly et al*., 2013b]. The net result is that bilateral (updip and downdip) propagation of swarm activity is observed in the early stages, where the fluid pressure increase dominates the nominal pressure gradient, and slip is triggered on an already stressed fault. However, the deep limb of activity falls quiet after the initial series of earthquakes, while the shallower limb persists (Figures 4d and 4h). This may indicate that the deep fluid pressure increase is brief—faulting would end as soon as the combined stress and fluid transfer from previous ruptures was insufficient to trigger failure on neighboring fault patches. The persistence of the shallower events suggests that fluid pressure continues to increase over a longer time in the shallower zone.

3.3. Frequency-Magnitude Distribution and *b* Value Variation

The Gutenberg-Richter *b* value is among the most commonly measured (and perhaps commonly abused) statistics in earthquake catalog studies. Here in deference to the fact that the *b* value alone is an incomplete description of the full frequency-magnitude distribution, we present a combination of *b* values and the corresponding distributions.

Figure 6 plots the full evolution of swarm magnitudes, for both catalog and newly detected events. Catalog events range from M_d −0.3 to M_w 3.5, while newly detected events extend down to M_{dext} −1.3, and form a

majority of total events up to *M* 0.3 (Figure 6c). The correction for expected incompleteness due to detector saturation during very high event rates (see section 2) has only a small effect on the overall *b* value estimate but a much larger effect on the 1000 event interval estimates that include the extraordinarily active day of 26 September. The corrected *b* value for the entire sequence is 0.74 ± 0.01 (Figure 6c), versus 0.70 ± 0.01 for the uncorrected distribution. Estimated *b* values from a moving 1000 event window (for events with $M \geq M_c$) begin at moderate values (for this swarm) of ~0.75, fall to a minimum early on 26 September, and then climb toward the overall peak above 0.9 late in the swarm (Figures 6b and 7).

Figure 7 plots event magnitude sequentially for all earthquakes above $M -0.4$. In this figure, the magnitude scale is transformed such that equal density of events is expected for a Gutenberg-Richter distribution with a specified *b* value. The transformed magnitude, M_{trans}, is calculated for all events of magnitude *M*:

$$M_{\text{trans}} = 10^{-bM}, \tag{6}$$

where we here assign $b = 0.7$, roughly the average value for the sequence. This is similar to the empirical transform proposed by *Agnew* [2015], yet because it is tied to a particular *b* value the variation proposed here retains additional information about deviations from the idealized power law distribution. As in *Agnew* [2015], we apply slight dithering when plotting the magnitudes for improved visibility in the figure. The overlaid color reflects the normalized density, smoothed using a continuous Gaussian kernel for a range of sequential events and magnitudes. Here we see that the variability underlying *b* value variations is more complex than variation of a single parameter—for instance, late in the swarm (beyond event 7000 in Figure 7), we observe deficits of event numbers from *M* 0 to *M* 0.2 and above *M* 0.7, compared to an idealized Gutenberg-Richter distribution with *b* value 0.7. In contrast, we see an excess of events below *M* 0 and between *M* 0.2 and *M* 0.6. At times, particularly during the July sequence, we see an apparent truncation of the distribution at larger magnitudes (supporting information Movie S3). This may reflect an additional length scale from the dimension of fluid pressure perturbation at this stage at the swarm. Similar truncation may be common in industrially induced seismicity [e.g., *Huang and Beroza*, 2015].

3.4. Origins of *b* Value Variations, Connections to Fault Structure

Although a *b* value does not capture complete information about the distribution of earthquake sizes, the best fitting *b* value of these distributions is a useful measure for comparisons over space or time. However, the exact cause of observed *b* value variations remains controversial. Several studies have suggested that *b* values are influenced by stress levels, in particular differential stress [e.g., *Scholz*, 1968; *Wyss*, 1973; *Schorlemmer et al*., 2005], while other studies have emphasized the role of material heterogeneity [e.g., *Mogi*, 1962; *Mori and Abercrombie*, 1997]. In natural faulting, these mechanisms are often intertwined, particularly when fluid pressure perturbations are involved [e.g., *Wiemer and McNutt*, 1997; *Wiemer et al*., 1998; *Bachmann et al*., 2012].

By combining *b* value analysis with high-resolution earthquake locations and magnitudes, we observe a clear correlation between the hypocentral structure and *b* value. Figure 8 compares the location patterns for the extreme values of our 1000 event window *b* values. The high and low *b* value times have very different hypocentral patterns. The low-*b* sequence (Figures 8a–8d) appears to activate a single, planar fault; in contrast, the high-*b* sequence (Figures 8e–8h) activates dozens of small, disparately oriented faults. Even assuming all individual faults produce similar *b* values, the small faults would exhibit a correspondingly small maximum magnitude, thus increasing the overall *b* value from a collection of these faults of various (but small) dimensions. This pattern of *b* value variation with hypocentral structure is persistent—supporting information Movie S3 shows the coupled evolution of hypocentral structure with frequency-magnitude distribution and *b* value for the entire sequence.

Other studies of seismic swarms have also shown *b* value variations with time, in both natural [e.g., *Wiemer et al*., 1998; *Hainzl and Fischer*, 2002; *Passarelli et al*., 2015] and induced [e.g., *Huang and Beroza*, 2015] environments; however, the sense of these fluctuations varies. *Wiemer et al.* [1998] found that *b* values around Mammoth Mountain increased relatively suddenly from ~0.8 to ~1.5 with the initiation of the 1989 swarm and remained elevated for at least several years, which the authors proposed was caused by persisting elevated fluid pressure. However, other swarms have shown decreasing *b* values. For example, the Vogtland/NW Bohemia swarms have exhibited patterns of decreasing *b* values from 1.4 to 0.8 in the 2000 swarm [*Hainzl and Fischer*, 2002] and 1.2 to 0.8 in the 2008–2009 swarm [*Hiemer et al*., 2012].

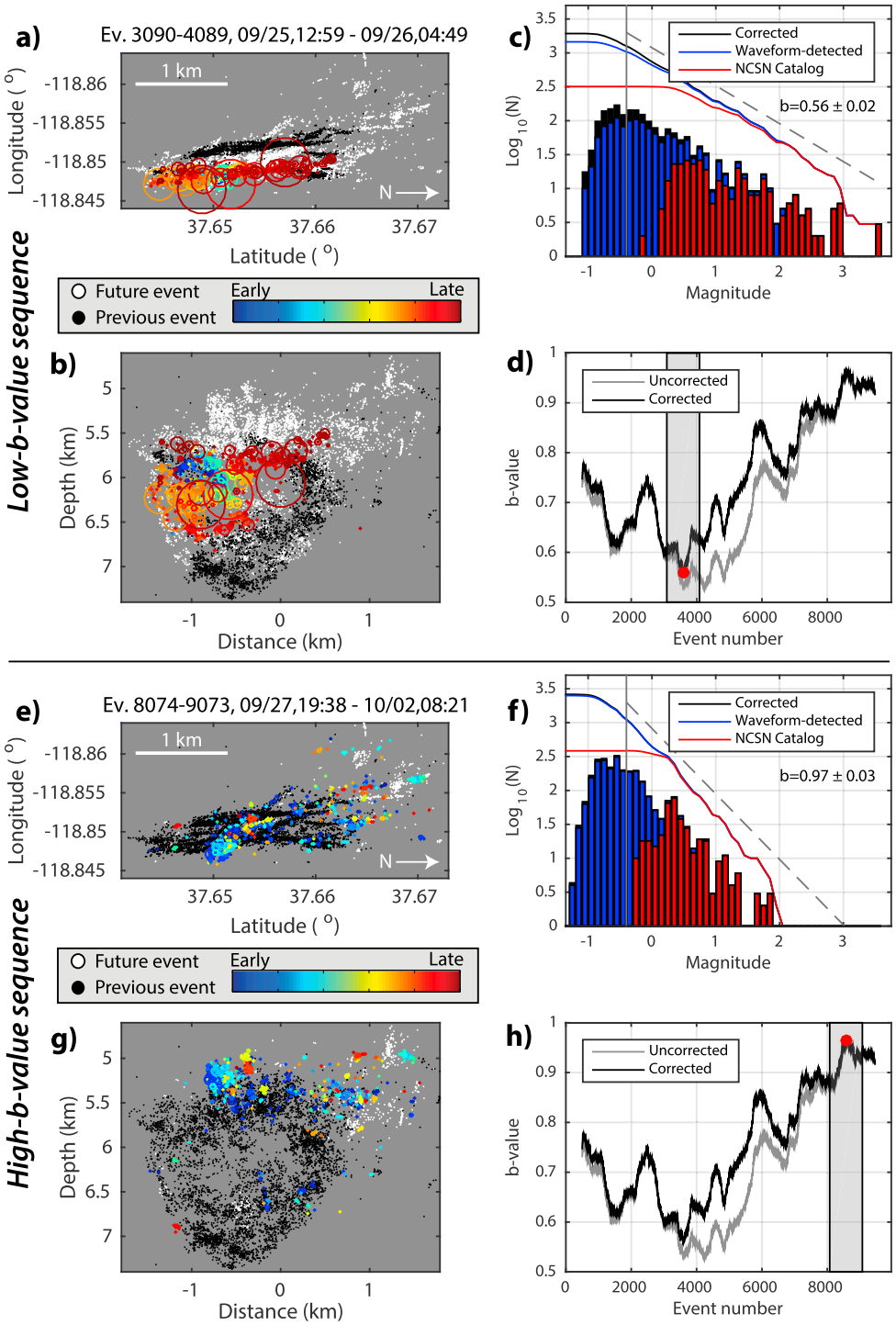

Figure 8. Comparison of a low-*b*-value sequence (Figures 8a–8d) and a high-*b*-value sequence (Figures 8e–8h), each containing 1000 events $\geq M_c = -0.4$. (a) Rotated map view. Colored events are those within the time period specified above the panel. Circles show estimated rupture dimensions for $M \geq 1$ earthquakes, assuming 3 MPa stress drop. (b) Corresponding south-north cross section. (c) Frequency-magnitude distribution, showing NCSN catalog events (red), newly detected events (blue), and a correction for times when the detector is blind (black). Lines show corresponding cumulative distributions (all earthquakes greater than or equal to a given magnitude). The *b* value (dashed line) is estimated using the corrected distribution. (d) The *b* value evolution for a 1000 event (above M_c) moving window (see Figure 7). Black line shows *b* value corrected for detector saturation time (see text); gray is uncorrected. Red dot and gray shaded width show the *b* value and window size corresponding to parts in Figures 8a–8c. (e–h) Same as Figures 8a–8d but for high-*b*-value sequence late in the swarm. For complete evolution of these plots during the swarm, see supporting information Movie S3.

Bachmann et al. [2012] reported a similar decrease for the Basel Enhanced Geothermal System project in 2006, going from $b = 1.6$ during injection to $b = 1.1$ after injection was halted, prompting the authors to propose that b value variations were caused by corresponding variations in pore pressure. Finally, other examples have shown more complex patterns. *Jenatton et al*. [2007] examined the 2003–2004 Ubaye (French Alps) swarm and reported b values peaking at ~1.5 during the climax of the swarm, much higher than values of ~1.0 early and late in the swarm. In contrast, *Passarelli et al*. [2015] examined the 2010–2014 Pollino, Italy, earthquake swarm and reported lowest b values (~1.0) associated with highest rates of swarm activity and higher b values (~1.4) associated with lower seismicity rates. We caution against overinterpretation of the absolute b values because of the magnitude scaling issues discussed earlier in the manuscript; relative variations should be more robust.

Differences in the temporal progression of b values in swarms may reflect differences in the spatial extent of fluid pressure increase, i.e., whether fluid injection is rapid and confined (such as Basel), or is more broadly distributed in space. Fluid injected rapidly at a single point would initially cause a large but very local pressure increase. Fault size within a random small volume would usually be small, and b value correspondingly large. Over time, the fluid pressure perturbation would diffuse outward, expanding the affected volume and increasing the likelihood of encountering larger faults, thus decreasing the observed b value. Similarly, confined injections of fluid into the NW Bohemia swarm areas might also explain decreasing b values for these swarms [*Hainzl and Fischer*, 2002; *Hiemer et al*., 2012]. On the other hand, a slower, broader increase in fluid pressure would produce a different pattern. Activation of separated structures early in the 2014 Long Valley swarm (May–July, see supporting information Movie S3) suggests that a somewhat broad increase in fluid pressure occurred for this swarm. In this situation, faults already nearest failure would be activated first—these would be faults that are favorably aligned in the regional stress field, which might fail with a relatively modest fluid pressure increase. Because of this, such faults may be most effective at confining fluid pressure within the fault zone, because failure occurs first along this orientation, rather than branching off to the sides. Such confinement, resulting in effectively 2-D rather than 3-D fluid diffusion, would also tend to preserve the fluid volume within the fault zone, making the process more effective at triggering continued failure on these larger faults. This process would also ensure that the fluid pressure perturbation preferentially encounters the extension of the same large fault.

As fluid pressure continued to increase, less favorably oriented structures could begin to be activated. As a consequence, fluid would no longer be confined in 2-D, since faults of various orientations would facilitate effectively 3-D flow. Because of this, a swarm may be less likely to sustain rupture on a single fault at higher-pressure perturbations; instead, fluid (and earthquakes) likely branches onto numerous, effectively smaller faults. This might explain the increasingly diffuse seismicity above ~5.7 km depth (Figures 1 and 4). Whether the fault size is limited by the region of perturbed fluid pressure or by the physical dimension of a preexisting structure is unclear, but either way, the effective dimension limits the magnitude of the largest event. Thus, high b values, which we observe to correspond to activation of many small faults, may be observed later in a swarm. These small faults will also tend to fail under low differential stress. Thus, our interpretation is partially consistent with that of *Bachmann et al*. [2012], but we propose that the coupled transition in the scale of faults activated by differing fluid pressure perturbations may be as important as the change in stress state itself.

Most of the above studies lack precise hypocentral locations, making it difficult to constrain associations between b values and fault structure. Extrapolating the results presented here; however, we propose that the inverse relationship between b values and fault dimension may be quite common. In the extreme, this correspondence is consistent with interpretations from industrial fluid injections, where hydraulic fracturing (creation of new faults) tends to produce a much higher b value (near 2.0) than activation of preexisting fractures (b value near 1.0) [*Maxwell et al*., 2009; *Wessels et al*., 2011; *Friberg et al*., 2014]. Dependence on the scale of the activated fault structure is also consistent with the results from natural faults in Southern California, where seismicity very near major faults exhibits a lower b value than seismicity farther from these faults [*Page et al*., 2011]. Because these major faults are typically inferred to be weak and thus slip under low resolved shear [e.g., *Zoback et al*., 1987] and differential [*Fialko et al*., 2005] stress, the lower b value on major faults is counter to the prediction based on differential stress alone [*Wyss*, 1973; *Scholz*, 2015].

In the 2014 Long Valley swarm, we also observe a correlation between high activity rate and low b value, similar to that reported for the 2010–2014 Pollino swarm [*Passarelli et al*., 2015]. Although precise hypocentral

locations were not available for the Pollino swarm, in Long Valley we see that the most active periods of the swarm correspond to times of rapidly cascading failure on a single fault. In contrast, lower rates (and higher *b* values) typically correspond with activation of numerous smaller faults of varying orientation. We infer that two main factors contribute to lower *b* values on a single, larger fault: (1) Individual, larger dimension faults have the potential to host larger magnitude events, compared with an array of smaller faults of various dimensions, and (2) individual approximately planar faults may have a more homogenous stress state than a collection of smaller faults with varying orientations. A possible third factor is incompleteness problems at small magnitudes during high event rate times—we correct for this here, but this is not common practice, and uncorrected *b* values are significantly lower during the highest activity rates (Figures 6–8). The high rate of activity is likely a direct consequence of a fault's proximity to failure and its ability to efficiently transmit stress and fluid pressure via the already ruptured zone to adjacent portions of the fault. Contrasting reports of higher *b* values during the highest swarm activity rates [e.g., *Jenatton et al*., 2007] might reflect cases where a sudden, local increase in fluid pressure activated small-scale faults.

4. Conclusions

The onset of swarm activity in Long Valley is modulated by episodes of resurgent dome inflation, even in cases where resultant stresses act counter to the sense of faulting [*Hill and Montgomery-Brown*, 2015], supporting the notion that inflation-related stresses are small relative to the regional stresses [*Prejean et al*., 2002]. For the 2014 swarm, stresses from inflation of the resurgent dome would have encouraged north striking left-lateral faulting, as observed in the swarm. However, probably a bigger effect would come from high-pressure hydrous fluids released by deep magma input that is likely driving the uplift. These hydrous fluids would then diffuse upward into the seismogenic crust thereby weakening faults within the existing fracture mesh. The time associated with this process might explain observed delays in the onset of swarm activity with respect to the onset of renewed inflation [*Hill*, 2006].

We infer from the high-resolution catalog produced here that this process of earthquake triggering by elevated fluid pressure was important in the 2014 Long Valley swarm. Based on the swarm hypocenter and frequency-magnitude evolution, we conclude that an overall gradual and somewhat broad (though nonuniform) fluid pressure increase affected the source region of the 31 May to 1 November 2014 Long Valley Caldera swarm. This can explain the separated fault segments activated early in the swarm (supporting information Movie S3). It is likely that the swarm gained momentum by a feedback mechanism, whereby gradual fluid pressure diffusion triggered localized faulting, which dramatically increased and accelerated fluid pressure diffusion. This process could be perpetuated as long as nearby faults remained stressed near enough to failure to be triggered by the available fluid pressure perturbation. Confinement of fluid during this stage within the (mostly) 2-D fault zone probably aided this process. As the swarm evolved, progressively less favorably oriented faults were probably activated. These later stage, somewhat poorly oriented structures may have failed under low resolved shear stress and also appear to be smaller, less-developed faults. These faults, failing over a range of orientations, may also be less effective at confining fluid pressure within the fault, reducing the likelihood of continued, sequential failure on the same fault.

High-resolution earthquake locations for the 2014 Long Valley Caldera swarm reveal that *b* values for this sequence have a close connection to the scale of faults activated, which depends both on the scales and orientations of preexisting structures, as well as on faulting history. In particular, we see here that single-fault activation tends to result in a low *b* value, while a multiple-fault activation results in a higher *b* value in aggregate, because of the limited size (and thus limited magnitude) of these small faults. This difference may reflect in part the degree of fluid confinement to an individual fault zone—when confined, the fluid pressure perturbation preferentially triggers earthquakes on the extension of the same relatively large fault. These distinct behaviors occur here over a spatial dimension of <1 km, which in many cases would be obscured by location uncertainty. This sequence can perhaps serve as a guide for other instances where precise locations are unavailable, since *b* values (event magnitudes) require fewer seismic stations and less elaborate processing to produce. In addition to previous interpretations that suggest differential stress or fluid pressure variations may cause *b* value variations, we hypothesize that these factors are interrelated with fault structure. In fact, fluid pressure and fluid pressure history may influence the populations of activated faults at any given time.

This swarm likely represents a natural analog to injection-induced seismicity, with similarly strong interactions between fluid pressure changes and faulting in both circumstances and rapid fluid diffusion in the wake of faulting. Differences in the temporal evolution of *b* values (e.g., falling versus rising) over the course of a sequence are likely coupled to the relative spatial and temporal confinement of fluid injection, interacting with preexisting faults.

Acknowledgments

Seismic stations used in this study are operated by the USGS, UC Berkeley, University of Nevada, Reno, and Caltech. Waveform data, metadata, and data products are freely available through the Northern California Earthquake Data Center (NCEDC), doi:10.7932/NCEDC, and the Southern California Earthquake Data Center (SCEDC), doi:10.7909/C3WD3xH1. We thank the network operators and seismic analysts for diligent work to maintain the network and process the data. Figure 1 was created using Generic Mapping Tools [*Wessel et al.*, 2002]. We thank Paul Hsieh, Shaul Hurwitz, Jeanne Hardebeck, Stephanie Prejean, Mitch Pitt, Emily Montgomery-Brown, Annemarie Baltay, and Tom Hanks for insightful discussions. We are grateful to Nicholas van der Elst for a detailed, constructive review of an earlier version of this manuscript. We also thank Editor Yehuda Ben-Zion and two anonymous reviewers for careful reviews and helpful comments that improved this manuscript.

References

Agnew, D. C. (2015), Equalized plot scales for exploring seismicity data, *Seismol. Res. Lett.*, *86*(5), 1412–1423.

Bachmann, C. E., S. Wiemer, B. P. Goertz-Allmann, and J. Woessner (2012), Influence of pore-pressure on the event-size distribution of induced earthquakes, *Geophys. Res. Lett.*, *39*, L09302, doi:10.1029/2012GL051480.

Bakun, W. H. (1984), Seismic moments, local magnitudes, and coda-duration magnitudes for earthquakes in central California, *Bull. Seismol. Soc. Am.*, *74*(2), 439–458.

Barton, C., D. Moos, and K. Tezuka (2009), Geomechanical wellbore imaging: Implications for reservoir fracture permeability, *AAPG Bull.*, *93*(11), 1551–1569.

Bender, B. (1983), Maximum likelihood estimation of *b* values for magnitude grouped data, *Bull. Seismol. Soc. Am.*, *73*(3), 831–851.

Benz, H. M., N. D. McMahon, R. C. Aster, D. E. McNamara, and D. B. Harris (2015), Hundreds of earthquakes per day: The 2014 Guthrie, Oklahoma, earthquake sequence, *Seismol. Res. Lett.*, *86*(5), 1318–1325.

Ben-Zion, Y., and L. Zhu (2002), Potency-magnitude scaling relations for southern California earthquakes with $1.0 < M_L < 7.0$, *Geophys. J. Int.*, *148*(3), F1–F5.

Chen, X., P. M. Shearer, and R. E. Abercrombie (2012), Spatial migration of earthquakes within seismic clusters in Southern California: Evidence for fluid diffusion, *J. Geophys. Res.*, *117*, B04301, doi:10.1029/2011JB008973.

Cleveland, K. M., and C. J. Ammon (2015), Precise relative earthquake magnitudes from cross correlation, *Bull. Seismol. Soc. Am.*, *105*(3), 1792–1796.

Cox, S. F. (2005), Coupling between deformation, fluid pressures, and fluid flow in ore-producing hydrothermal systems at depth in the crust, in *Economic Geology 100th Anniversary Volume*, pp. 39–75, Soc. of Econ. Geol., Littleton, Colo.

Cox, S. F. (2010), The application of failure mode diagrams for exploring the roles of fluid pressure and stress states in controlling styles of fracture-controlled permeability enhancement in faults and shear zones, *Geofluids*, *10*, 217–233.

Dreger, D. S., H. Tkalčić, and M. Johnston (2000), Dilational processes accompanying earthquakes in the Long Valley Caldera, *Science*, *288*(5463), 122–125.

Eaton, J. P. (1992), Determination of amplitude and duration magnitudes and site residuals from short-period seismographs in Northern California, *Bull. Seismol. Soc. Am.*, *82*(2), 533–579.

Ellsworth, W. L. (2013), Injection-induced earthquakes, *Science*, *341*(6142), 1225942.

Fialko, Y., L. Rivera, and H. Kanamori (2005), Estimate of differential stress in the upper crust from variations in topography and strike along the San Andreas Fault, *Geophys. J. Int.*, *160*(2), 527–532.

Fischer, T., and A. Guest (2011), Shear and tensile earthquakes caused by fluid injection, *Geophys. Res. Lett.*, *38*, L05307, doi:10.1029/2010GL045447.

Fischer, T., J. Horálek, P. Hrubcová, V. Vavryčuk, K. Bräuer, and H. Kämpf (2014), Intra-continental earthquake swarms in West-Bohemia and Vogtland: A review, *Tectonophysics*, *611*, 1–27.

Foulger, G. R., B. R. Julian, D. P. Hill, A. M. Pitt, P. E. Malin, and E. Shalev (2004), Non-double-couple microearthquakes at Long Valley Caldera, California, provide evidence for hydraulic fracturing, *J. Volcanol. Geotherm. Res.*, *132*(1), 45–71.

Fournier, R. O. (1999), Hydrothermal processes related to movement of fluid from plastic into brittle rock in the magmatic-epithermal environment, *Econ. Geol.*, *94*(8), 1193–1211.

Friberg, P. A., G. M. Besana-Ostman, and I. Dricker (2014), Characterization of an earthquake sequence triggered by hydraulic fracturing in Harrison County, Ohio, *Seismol. Res. Lett.*, *85*(6), doi:10.1785/0220140127.

Frohlich, C. (2012), Two-year survey comparing earthquake activity and injection-well locations in the Barnett Shale, Texas, *Proc. Natl. Acad. Sci. U.S.A.*, *109*(35), 13,934–13,938.

Gibbons, S. J., and F. Ringdal (2006), The detection of low magnitude seismic events using array-based waveform correlation, *Geophys. J. Int.*, *165*(1), 149–166.

Gudmundsson, A., N. Lecoeur, N. Mohajeri, and T. Thordarson (2014), Dike emplacement at Bardarbunga, Iceland, induces unusual stress changes, caldera deformation, and earthquakes, *Bull. Volcanol.*, *76*(10), 1–7.

Gutenberg, B., and C. Richter (1942), Earthquake magnitude, intensity, energy, and acceleration, *Bull. Seismol. Soc. Am.*, *32*(3), 163–191.

Hainzl, S. (2004), Seismicity patterns of earthquake swarms due to fluid intrusion and stress triggering, *Geophys. J. Int.*, *159*(3), 1090–1096.

Hainzl, S., and T. Fischer (2002), Indications for a successively triggered rupture growth underlying the 2000 earthquake swarm in Vogtland/NW Bohemia, *J. Geophys. Res.*, *107*(B12), 2338, doi:10.1029/2002JB001865.

Hainzl, S., T. Fischer, and T. Dahm (2012), Seismicity-based estimation of the driving fluid pressure in the case of swarm activity in Western Bohemia, *Geophys. J. Int.*, *191*(1), 271–281.

Hanks, T. C., and D. M. Boore (1984), Moment-magnitude relations in theory and practice, *J. Geophys. Res.*, *89*, 6229–6235.

Hanks, T. C., and H. Kanamori (1979), A moment magnitude scale, *J. Geophys. Res.*, *84*, 2348–2350.

Healy, J. H., W. W. Rubey, D. T. Griggs, and C. B. Raleigh (1968), The Denver earthquakes, *Science*, *161*(3848), 1301–1310.

Hiemer, S., D. Roessler, and F. Scherbaum (2012), Monitoring the West Bohemian earthquake swarm in 2008/2009 by a temporary small-aperture seismic array, *J. Seismol.*, *16*(2), 169–182.

Hildreth, W. (2004), Volcanological perspectives on Long Valley, Mammoth Mountain, and Mono Craters: Several contiguous but discrete systems, *J. Volcanol. Geotherm. Res.*, *136*(3), 169–198.

Hill, D. P. (1977), A model for earthquake swarms, *J. Geophys. Res.*, *82*, 1347–1352.

Hill, D. P. (1993), A note on ambient pore pressure, fault-confined pore pressure, and apparent friction, *Bull. Seismol. Soc. Am.*, *83*(2), 583–586.

Hill, D. P. (2006), Unrest in Long Valley Caldera, California, 1978–2004, *Geol. Soc. London Spec. Publ.*, *269*(1), 1–24.

Hill, D. P., and E. K. Montgomery-Brown (2015), Long Valley Caldera and the UCERF depiction of Sierra Nevada range-front faults, *Bull. Seismol. Soc. Am.*, *105*(6), 3189–3195, doi:10.1785/0120150149.

Hill, D. P., and S. Prejean (2005), Magmatic unrest beneath Mammoth Mountain, California, *J. Volcanol. Geotherm. Res.*, *146*(4), 257–283.
Hill, D. P., J. O. Langbein, and S. Prejean (2003), Relations between seismicity and deformation during unrest in Long Valley Caldera, California, from 1995 through 1999, *J. Volcanol. Geotherm. Res.*, *127*(3), 175–193.
Horton, S. (2012), Disposal of hydrofracking waste fluid by injection into subsurface aquifers triggers earthquake swarm in central Arkansas with potential for damaging earthquake, *Seismol. Res. Lett.*, *83*(2), 250–260.
Huang, Y., and G. C. Beroza (2015), Temporal variation in the magnitude-frequency distribution during the Guy-Greenbrier earthquake sequence, *Geophys. Res. Lett.*, *42*, 6639–6646, doi:10.1002/2015GL065170.
Hubbert, M. K., and W. W. Rubey (1959), Role of fluid pressure in mechanics of overthrust faulting I. Mechanics of fluid-filled porous solids and its application to overthrust faulting, *Geol. Soc. Am. Bull.*, *70*(2), 115–166.
Ingebritsen, S. E., and C. E. Manning (2010), Permeability of the continental crust: Dynamic variations inferred from seismicity and metamorphism, *Geofluids*, *10*(1–2), 193–205.
Ishimoto, M., and K. Iida (1939), Observations of earthquakes registered with the microseismograph constructed recently, *Bull. Earthquake Res. Inst.*, *17*, 443–478.
Jenatton, L., R. Guiguet, F. Thouvenot, and N. Daix (2007), The 16,000-event 2003–2004 earthquake swarm in Ubaye (French Alps), *J. Geophys. Res.*, *112*, B11304, doi:10.1029/2006JB004878.
Kagan, Y. Y. (1991), Seismic moment distribution, *Geophys. J. Int.*, *106*(1), 123–134.
Lewicki, J. L., G. E. Hilley, D. R. Shelly, J. C. King, J. P. McGeehin, M. Mangan, and W. C. Evans (2014), Crustal migration of CO_2-rich magmatic fluids recorded by tree-ring radiocarbon and seismicity at Mammoth Mountain, CA, USA, *Earth Planet. Sci. Lett.*, *390*, 52–58.
Linde, A. T., M. T. Gladwint, M. J. Johnston, R. L. Gwythert, and R. G. Bilham (1996), A slow earthquake sequence on the San Andreas Fault, *Nature*, *383*, 5.
Martens, H. R., and R. S. White (2013), Triggering of microearthquakes in Iceland by volatiles released from a dyke intrusion, *Geophys. J. Int.*, *194*, 1738–1754.
Marzocchi, W., and L. Sandri (2003), A review and new insights on the estimation of the b-value and its uncertainty, *Ann. Geophys.*, *46*(6), 1271–1282.
Maxwell, S. C., M. Jones, R. Parker, S. Miong, S. Leaney, D. Dorval, D. D'Amico, J. Logel, E. Anderson, and K. Hammermaster (2009), Fault activation during hydraulic fracturing, 2009 SEG Annual Meeting, Soc. of Explor. Geophys., Houston, Tex., 25-30 Oct.
McClure, M. W., and R. N. Horne (2011), Investigation of injection-induced seismicity using a coupled fluid flow and rate/state friction model, *Geophysics*, *76*(6), WC181–WC198.
Mogi, K. (1962), Magnitude-frequency relation for elastic shocks accompanying fractures of various materials and some related problems in earthquakes (2nd paper), *Bull. Earthquake Res. Inst. Univ. Tokyo*, *40*, 831–853.
Mogi, K. (1963), Some discussions on Aftershocks, foreshocks and earthquake swarms—The fracture of a semi-infinite body caused by an inner stress origin and its relation to the earthquake phenomena (3rd paper), *Bull. Earthquake Res. Inst. Univ. Tokyo*, *41*, 615–658.
Montgomery-Brown, E. K., C. W. Wicks, P. F. Cervelli, J. O. Langbein, J. L. Svarc, D. R. Shelly, D. P. Hill, and M. Lisowski (2015), Renewed inflation of Long Valley Caldera, California (2011 to 2014), *Geophys. Res. Lett.*, *42*, 5250–5257, doi:10.1002/2015GL064338.
Mori, J., and R. E. Abercrombie (1997), Depth dependence of earthquake frequency-magnitude distributions in California: Implications for rupture initiation, *J. Geophys. Res.*, *102*, 15–081.
Ozawa, S., S. Miyazaki, Y. Hatanaka, T. Imakiire, M. Kaidzu, and M. Murakami (2003), Characteristic silent earthquakes in the eastern part of the Boso peninsula, Central Japan, *Geophys. Res. Lett.*, *30*(6), 1283, doi:10.1029/2002GL016665.
Page, M. T., D. Alderson, and J. Doyle (2011), The magnitude distribution of earthquakes near Southern California faults, *J. Geophys. Res.*, *116*, B12309, doi:10.1029/2010JB007933.
Parotidis, M., E. Rothert, and S. A. Shapiro (2003), Pore-pressure diffusion: A possible triggering mechanism for the earthquake swarms 2000 in Vogtland/NW-Bohemia, central Europe, *Geophys. Res. Lett.*, *30*(20), 2075, doi:10.1029/2003GL018110.
Passarelli, L., S. Hainzl, S. Cesca, F. Maccaferri, M. Mucciarelli, D. Roessler, F. Corbi, T. Dahm, and E. Rivalta (2015), Aseismic transient driving the swarm-like seismic sequence in the Pollino range, Southern Italy, *Geophys. J. Int.*, *201*(3), 1553–1567.
Prejean, S., W. Ellsworth, M. Zoback, and F. Waldhauser (2002), Fault structure and kinematics of the Long Valley Caldera region, California, revealed by high-accuracy earthquake hypocenters and focal mechanism stress inversions, *J. Geophys. Res.*, *107*(B12), 2355, doi:10.1029/2001JB001168.
Prejean, S., A. Stork, W. Ellsworth, D. Hill, and B. Julian (2003), High precision earthquake locations reveal seismogenic structure beneath Mammoth Mountain, California, *Geophys. Res. Lett.*, *30*(24), 2247, doi:10.1029/2003GL018334.
Prejean, S. G., and W. L. Ellsworth (2001), Observations of earthquake source parameters at 2 km depth in the Long Valley Caldera, eastern California, *Bull. Seismol. Soc. Am.*, *91*(2), 165–177.
Rubinstein, J. L., and W. L. Ellsworth (2010), Precise estimation of repeating earthquake moment: Example from Parkfield, California, *Bull. Seismol. Soc. Am.*, *100*(5A), 1952–1961.
Schaff, D. P., and P. G. Richards (2014), Improvements in magnitude precision, using the statistics of relative amplitudes measured by cross correlation, *Geophys. J. Int.*, *197*(1), 335–350.
Schaff, D. P., G. H. Bokelmann, W. L. Ellsworth, E. Zanzerkia, F. Waldhauser, and G. C. Beroza (2004), Optimizing correlation techniques for improved earthquake location, *Bull. Seismol. Soc. Am.*, *94*(2), 705–721.
Scholz, C. H. (1968), The frequency-magnitude relation of microfracturing in rock and its relation to earthquakes, *Bull. Seismol. Soc. Am.*, *58*(1), 399–415.
Scholz, C. H. (2015), On the stress dependence of the earthquake b value, *Geophys. Res. Lett.*, *42*, 1399–1402, doi:10.1002/2014GL062863.
Schorlemmer, D., S. Wiemer, and M. Wyss (2005), Variations in earthquake-size distribution across different stress regimes, *Nature*, *437*(7058), 539–542.
Seccia, D., C. Chiarabba, P. De Gori, I. Bianchi, and D. P. Hill (2011), Evidence for the contemporary magmatic system beneath Long Valley Caldera from local earthquake tomography and receiver function analysis, *J. Geophys. Res.*, *116*, B12314, doi:10.1029/2011JB008471.
Segall, P., E. K. Desmarais, D. Shelly, A. Miklius, and P. Cervelli (2006), Earthquakes triggered by silent slip events on Kīlauea Volcano, Hawaii, *Nature*, *442*(7098), 71–74.
Shapiro, S. A., E. Huenges, and G. Borm (1997), Estimating the crust permeability from fluid-injection-induced seismic emission at the KTB site, *Geophys. J. Int.*, *131*(2), F15–F18.
Shelly, D. R., and D. P. Hill (2011), Migrating swarms of brittle-failure earthquakes in the lower crust beneath Mammoth Mountain, California, *Geophys. Res. Lett.*, *38*, L20307, doi:10.1029/2011GL049336.
Shelly, D. R., S. C. Moran, and W. A. Thelen (2013a), Evidence for fluid-triggered slip in the 2009 Mount Rainier, Washington earthquake swarm, *Geophys. Res. Lett.*, *40*, 1506–1512, doi:10.1002/grl.50354.

Shelly, D. R., D. P. Hill, F. Massin, J. Farrell, R. B. Smith, and T. A. Taira (2013b), A fluid-driven earthquake swarm on the margin of the Yellowstone caldera, *J. Geophys. Res. Solid Earth*, *118*, 4872–4886, doi:10.1002/jgrb.50362.
Shelly, D. R., T. A. Taira, S. G. Prejean, D. P. Hill, and D. S. Dreger (2015), Fluid-faulting interactions: Fracture-mesh and fault-valve behavior in the February 2014 Mammoth Mountain, California, earthquake swarm, *Geophys. Res. Lett.*, *42*, 5803–5812, doi:10.1002/2015GL064325.
Shi, Y., and B. A. Bolt (1982), The standard error of the magnitude-frequency *b* value, *Bull. Seismol. Soc. Am.*, *72*(5), 1677–1687.
Sibson, R. H. (1981), Fluid flow accompanying faulting: Field evidence and models, in *Earthquake Prediction*, pp. 593–603, AGU, Washington, D. C.
Sibson, R. H. (1985), A note on fault reactivation, *J. Struct. Geol.*, *7*(6), 751–754.
Sibson, R. H. (1987), Earthquake rupturing as a mineralizing agent in hydrothermal systems, *Geology*, *15*(8), 701–704.
Sibson, R. H. (1996), Structural permeability of fluid-driven fault-fracture meshes, *J. Struct. Geol.*, *18*(8), 1031–1042.
Sibson, R. H. (2001), Seismogenic framework for hydrothermal transport and ore deposition, *Rev. Econ. Geol.*, *14*, 25–50.
Terakawa, T., C. Hashimoto, and M. Matsu'ura (2013), Changes in seismic activity following the 2011 Tohoku-oki earthquake: Effects of pore fluid pressure, *Earth Planet. Sci. Lett.*, *365*, 17–24.
Tinti, S., and F. Mulargia (1987), Confidence intervals of *b* values for grouped magnitudes, *Bull. Seismol. Soc. Am.*, *77*(6), 2125–2134.
Uhrhammer, R. A., M. Hellweg, K. Hutton, P. Lombard, A. W. Walters, E. Hauksson, and D. Oppenheimer (2011), California Integrated Seismic Network (CISN) local magnitude determination in California and vicinity, *Bull. Seismol. Soc. Am.*, *101*(6), 2685–2693.
Ukawa, M., and H. Tsukahara (1996), Earthquake swarms and dike intrusions off the east coast of Izu Peninsula, central Japan, *Tectonophysics*, *253*(3), 285–303.
Utsu, T. (1966), A statistical significance test of the difference in b-value between two earthquake groups, *J. Phys. Earth*, *14*(2), 37–40.
Utsu, T. (1999), Representation and analysis of the earthquake size distribution: A historical review and some new approaches, *Pure Appl. Geophys.*, *155*, 509–535.
Vavryčuk, V. (2002), Non-double-couple earthquakes of 1997 January in West Bohemia, Czech Republic: Evidence of tensile faulting, *Geophys. J. Int.*, *149*(2), 364–373.
Vavryčuk, V., F. Bouchaala, and T. Fischer (2013), High-resolution fault image from accurate locations and focal mechanisms of the 2008 swarm earthquakes in West Bohemia, Czech Republic, *Tectonophysics*, *590*, 189–195.
Waite, G. P., and R. B. Smith (2002), Seismic evidence for fluid migration accompanying subsidence of the Yellowstone caldera, *J. Geophys. Res.*, *107*(B9), 2177, doi:10.1029/2001JB000586.
Waldhauser, F., and W. L. Ellsworth (2000), A double-difference earthquake location algorithm: Method and application to the northern Hayward fault, California, *Bull. Seismol. Soc. Am.*, *90*(6), 1353–1368.
Waldhauser, F., and D. P. Schaff (2008), Large-scale relocation of two decades of Northern California seismicity using cross-correlation and double-difference methods, *J. Geophys. Res.*, *113*, B08311, doi:10.1029/2007JB005479.
Wessel, P., W. H. F. Smith, R. Scharroo, J. Luis, and F. Wobbe (2013), Generic mapping tools: Improved version released, *Eos Trans. AGU*, *94*(45), 409–410, doi:10.1002/2013EO450001.
Wessels, S., M. Kratz, and A. De La Pena (2011), Identifying fault activation during hydraulic stimulation in the Barnett shale: Source mechanisms, *b* values, and energy release analyses of microseismicity 2011 SEG Annual Meeting, Soc. of Explor. Geophys., San Antonio, Tex., 18-23 Sept.
White, R. S., J. Drew, H. R. Martens, J. Key, H. Soosalu, and S. S. Jakobsdóttir (2011), Dynamics of dyke intrusion in the mid-crust of Iceland, *Earth Planet. Sci. Lett.*, *304*(3), 300–312.
Wiemer, S., and S. R. McNutt (1997), Variations in the frequency-magnitude distribution with depth in two volcanic areas: Mount St. Helens, Washington, and Mt. Spurr, Alaska, *Geophys. Res. Lett.*, *24*, 189–192.
Wiemer, S., and M. Wyss (2000), Minimum magnitude of completeness in earthquake catalogs: Examples from Alaska, the western United States, and Japan, *Bull. Seismol. Soc. Am.*, *90*, 859.
Wiemer, S., S. R. McNutt, and M. Wyss (1998), Temporal and three-dimensional spatial analyses of the frequency–magnitude distribution near Long Valley Caldera, California, *Geophys. J. Int.*, *134*(2), 409–421.
Woessner, J., and S. Wiemer (2005), Assessing the quality of earthquake catalogues: Estimating the magnitude of completeness and its uncertainty, *Bull. Seismol. Soc. Am.*, *95*(2), 684–698.
Wyss, M. (1973), Towards a physical understanding of the earthquake frequency distribution, *Geophys. J. Int.*, *31*(4), 341–359.
Zaliapin, I., and Y. Ben-Zion (2013), Earthquake clusters in southern California II: Classification and relation to physical properties of the crust, *J. Geophys. Res. Solid Earth*, *118*, 2865–2877, doi:10.1002/jgrb.50178.
Zoback, M. D., et al. (1987), New evidence on the state of stress of the San Andreas Fault system, *Science*, *238*(4830), 1105–1111.